1 **Manuscript Number 8568R1   Correction date 2022.10.24   Word Count:**

2 **5348**

Synthesis of boehmite-type GaOOH: a new polymorph of Ga oxyhydroxide and geochemical implications

5 Meng Liu[a,b], Wei Yin[a,b], Hao-Fan Jiang[a,b], Yu-Han Wang[a,b], Qi-Tao Hu[a,b], Tian-Lei Zhao[a,b],

6 Qi-Zhi Yao[c,*], Sheng-Quan Fu[d] and Gen-Tao Zhou[a,b,e,*]

7 [a] Deep Space Exploration Laboratory/School of Earth and Space Sciences, University of Science

8 and Technology of China, Hefei 230026, China

9 [b] CAS Key Laboratory of Crust-Mantle Materials and Environments, School of Earth and

10 Space Sciences, University of Science and Technology of China, Hefei 230026, China

11 [c] School of Chemistry and Materials Science, University of Science and Technology of China,

12 Hefei 230026, China

13 [d] Hefei National Laboratory for Physical Sciences at the Microscale, University of Science

14 and Technology of China, Hefei 230026, China

15 [e] CAS Center for Excellence in Comparative Planetology, Hefei 230026, China

16 Corresponding authors: Dr. Qi-Zhi Yao, Prof. Dr. Gen-Tao Zhou

17 Tel.: 86 551 63600533

18 Email: qzyao@ustc.edu.cn, gtzhou@ustc.edu.cn

Abstract

19

20   Gallium (Ga) and aluminum (Al) belong to group IIIA elements in the periodic table.

21 They show a coupled geochemical behavior in most natural systems, and are considered as

22 "geochemical partners". However, compared with the principal oxyhydroxides of Al in nature,

23 gibbsite ($Al(OH)_3$), boehmite (γ-AlOOH), and diaspore (α-AlOOH), only the analogs

24 söhngeite ($Ga(OH)_3$) and tsumgallite (α-GaOOH) were reported. In this work, boehmite-type

25 GaOOH (γ-GaOOH), a new polymorph of GaOOH, was synthesized for the first time using

26 boehmite (γ-AlOOH) as a template. The synthesized γ-GaOOH was characterized by a series

27 of techniques including X-ray diffraction (XRD), high angle annular dark-field scanning

28 transmission electron microscopy (HAADF-STEM) and selected area electron diffraction

29 (SAED). Furthermore, a model based on the boehmite structure was successfully applied to

30 define the γ-GaOOH structure by the Rietveld method. Results from sample characterization

31 and structural refinement support the successful synthesis of boehmite-type GaOOH, and thus

32 it is referred to as γ-GaOOH. The synthesis of γ-GaOOH in laboratory is valuable to

33 understanding the Ga geochemistry and its enrichment process in Ga-rich boehmite in coal

34 and bauxite.

35   **Keywords:** gallium, boehmite analog, γ-GaOOH, template synthesis, Ga geochemistry

Introduction

36

37   Gallium (Ga) is an important strategic resource and has been widely used in the

38   manufacturing of semiconductor devices (Ji et al., 2021), such as integrated circuits (Zhan et

39   al., 2020), optoelectronics (Sutter et al., 2020), photovoltaic solar cells (Ramanujam et al.,

40   2017), and many modern high-tech fields, including 5G communication (Lv et al., 2019) and

41   Internet of things (Braniste et al., 2020), etc. The global Ga demand is projected to increase

42   12-fold by 2050 (Eheliyagoda et al., 2019). Thus, the prospecting and exploitation of Ga

43   resources in nature have become ever important for meeting the increasing demand for Ga

44   (Gladyshev et al., 2015). However, Ga usually occurs as a trace element in a range of minerals

45   (e.g., bauxite and Zn ores), and therefore, no mines endowed of Ga as main commodities have

46   been discovered so far (Shao et al., 2018; Ji et al., 2020; Zhan et al., 2020). As a consequence,

47   the bulk of the global Ga derived from bauxite (e.g., karst-type bauxites) and Zn ores (e.g.,

48   Mississippi Valley Type) is exploited as a by-product from Al and Zn production (Lu et al.,

49   2017; Xue et al., 2019; U.S. Geological Survey, 2021). According to Seredin et al. (2013), the

50   average Ga contents in bauxite are approximately 50 $\mu g \cdot g^{-1}$, with a total amount estimated

51   over 1 billion kg (Lu et al., 2017), which contribute almost 90% of the annual global Ga

52   supply (Maarefvand et al., 2020). The identified worldwide Zn ores account for about 0.1

53   billion kg of Ga (Corathers et al., 2017), which correspond to nearly 10% of the global

54   production of Ga (Frenzel et al., 2016). As the by-product of Zn and Al production, the Ga

55   production is inevitably affected by the exploitation of the main commodity (Frenzel et al.,

56   2016). Nevertheless, in the past two decades, the enrichment of Ga was also discovered in

57   coal, with some of them far higher than the industrial grade (30 $\mu g \cdot g^{-1}$) (Dai et al., 2006a,

58   2006b, 2008, 2012; Zhou et al., 2010; Zhao et al., 2009; Wang et al., 2011; Mastalerz et al.,

59   2012; Sun et al., 2013; Qin et al. 2015; Qiao et al., 2016; Saikia et al., 2016; Shao et al., 2018).

60   According to a rough estimate, coal deposits account for approximately 10 billion kg of Ga

61   (Zhao et al., 2020), which represent almost ten times the amount of Ga estimated in bauxite

62   and Zn ores. However, so far, the reports about Ga exploitation from coal are rare and the

63   yield is not high (Bielowicz et al., 2020).

64   In natural systems, Ga is found primarily in trivalent oxidation state (Schulz et al., 2017).

65   Ga^{3+} can exist in the form of $Ga(OH)_3$, due to its metastability, which would spontaneously

66   transform into α-GaOOH (Wang et al., 2011). Ga and Al have similar geochemical behavior

67   resulting from similarities in oxidation state, amphotericity, coordination, and ionic radius

68   (Rytuba et al., 2003). Therefore, during weathering of aluminosilicate-rich rocks (e.g., tephra

69   and granite), they both behave as immobile elements and are enriched in newly formed

70   oxyhydroxides species (Rytuba et al., 2003). As a consequence, Ga often occurs in Al-bearing

71   minerals (Dai et al., 2006a; Kato et al., 2017). Compared with gibbsite ($Al(OH)_3$), diaspore

72   (α-AlOOH) and boehmite (γ-AlOOH), only the analogs söhngeite ($Ga(OH)_3$) and tsumgallite

73   (α-GaOOH) were reported. In particular, α-GaOOH is isostructural with α-AlOOH, and they

74   are thermodynamically stable oxyhydroxides of Ga and Al under ambient conditions (Foley et

75   al, 2017). It appears that Ga should be more readily enriched in diaspore rather than boehmite

76   and gibbsite in the form of α-GaOOH. However, Dai et al. (2006a) suggested that Ga in coals

77   from the Heidaigou Mine exists mainly in boehmite rather than other Al-bearing minerals

78   such as diaspore. Except for Heidaigou Mine, Ga enriched in boehmite were also reported by

79   some other studies (Dai et al., 2008, 2012; Wang et al., 2011; Sun et al., 2013; Schulte et al.,

80   2014; Abedini et al., 2019). However, up to now, the enrich process and occurrence of Ga in

81   boehmite are still unclear.

82   In this work, boehmite was used as a template to induce the precipitation of

83   boehmite-type GaOOH (γ-GaOOH), and the structure of γ-GaOOH was characterized by

84   several methods. The successful synthesis of γ-GaOOH not only enriches the family of Ga

85   compounds, but also provides a new perspective of Ga geochemistry and occurrence in

86   natural systems.

Materials and methods

87

Materials

88

89   All chemicals used in this work were of analytical grade and were used as received.

90   Purified water purchased from Hangzhou Wahaha Group Co, Ltd was used in all the

4

91   experiments. NaOH (≥96%, CAS No.1310-73-2), HCl solution (36%-38%, CAS

92   No.7647-01-0), $Ga(NO_3)_3 \cdot xH_2O$ (99.9%, CAS No.69365-72-6), $Al(NO_3)_3 \cdot 9H_2O$ (>99%, CAS

93   No.7784-27-2) and $(NH_2)_2CO$ (≥99%, CAS No.57-13-6) were purchased from Sinopharm

94   Chemical Reagent Co., Ltd.

Preparation of boehmite-type GaOOH (γ-GaOOH)

96   Boehmite were first synthesized following the procedure of Dubey et al., (2017), and the

97   detailed experimental process was depicted in Supporting Information (SI). Boehmite-type

98   GaOOH (γ-GaOOH) was prepared with the boehmite as a template at pH 2.0 and 70 °C in

99   solution. Firstly, the Ga^{3+} solution was prepared by dissolving 73 mg $Ga(NO_3)_3 \cdot xH_2O$ with

100   100 mL purified water, and the initial pH of the Ga^{3+} solution was adjusted to pH 2.0 by a 0.1

101   mol L^{-1} of HCl solution. Subsequently, 0.1 g of boehmite powder was dispersed into the Ga^{3+}

102   solution. After ultrasound treatment for 5 min, the suspension was transferred to a sealed glass

103   bottle, and let stand in a 70 °C oven for 3 days. The product was collected by centrifugation,

104   washed with purified water three times, and dried in a 30 °C vacuum oven for 24 h. For

105   comparison, the reaction of boehmite, diaspore, gibbsite, corundum or without template in

106   Ga^{3+} solution with broader temperature conditions (60, 80 and 150 °C) were also conducted

107   by the same procedures.

Sample characterization

109   X-ray diffraction (XRD) analysis of the samples was conducted using a Japan Rigaku

110   Smart Lab at 40 kV and 200 mA equipped with graphite-monochromatized Cu Kα irradiation

111   (λ = 1.541841 Å) with a step of 0.01° and scanning rate of 0.03° s^{-1}, and a Ni filter was used

112   to remove K_β radiation. The crystal structure was verified and refined using the Rietveld

113   method using general structure analysis system (GSAS) software with EXPGUI interface.

114   Structural refinements of the two phases in the product were conducted using the boehmite

115   structure as the input model, with space group *Cmcm* and initial lattice parameters of a =

116   3.6936 Å, b = 12.2140 Å, and c = 2.8679 Å (Christoph et al.,1979). The background of the

117   XRD pattern was simulated using the function of "Chebyschev polynomial of the first kind"

118 with 36 coefficients. The peak profile was modeled by "CW profile function 3" in the GSAS

119 software, which is a variation of the pseudo-voigt function. No restraints or constraints were

120 adopted. The zero-error was not considered because the Japan Rigaku SmartLab X-ray

121 diffractometer has been corrected using standard samples (silicon powder) regularly. In

122 addition, the isotropic atomic displacement parameters were varied in the refinement process.

123 Typically, in the XRD pattern, the main phase is γ-AlOOH. Hence, the γ-AlOOH structure

124 was refined first. As for γ-GaOOH, the scale factor (phase fraction) was firstly adjusted to a

125 suitable value. Then, the unit cell parameters were refined. In the following refinement

126 process, the scale factor and unit cell parameters were varied together. In the next step, the

127 peak profile was refined to obtain a good peak shape. In the final step, the atomic positions

128 and the isotropic displacement parameters was refined.

129   The morphology of the samples was characterized by a cold field-emission scanning

130 electron microscopy (FESEM, HITACHI SU8220). Transmission electron microscopy (TEM)

131 and selected area electron diffraction (SAED) analyses were performed on a JEM-2100Plus

132 transmission electron microscope with an accelerating voltage of 200 kV. Probe

133 aberration-corrected JEOL ARM-200F field emission transmission electron microscope was

134 employed to obtain the high angle annular dark-field scanning transmission electron

135 microscopy (HAADF-STEM) images and element mappings of the samples with an

136 accelerating voltage of 200 kV.

Results and Discussion

Characterization of boehmite-type GaOOH (γ-GaOOH)

139   After introducing the template boehmite in Ga^{3+} solution, the suspension was reacted at

140 70 °C for 3 days. The morphology and texture of the product were characterized by TEM. As

141 shown in Fig. 1a, a definite contrast difference is observable among the nanoplates, hinting

142 towards the presence of two different phases in the product. Comparing with the TEM images

143 of the template boehmite (Figs. 1b and S1c), the nanoplates with the lighter contrast (area 1 in

144 Fig.1a) should be boehmite template. Interestingly, the nanoplates with the darker contrast

145 (area 2 in Fig.1a) are orientationally attached to the boehmite crystal, forming a

146   heterostructure, and the boehmite template was partially dissolved relative to the boehmite

147   prototype (Figs. 1b and S1c). Fig. 1c-f shows STEM-EDS mappings and corresponding EDS

148   spectra collected from the product. The EDX mappings revealed their biphasic nature of the

149   synthesized product. Specifically, the EDS spectrum (Fig. 1e) collected from the nanoplate

150   with the lighter contrast detected a composition matching with boehmite (i.e., 30 at. % of Al

151   and 68 at. % of O, with O/Al atomic ratio close to 2). The observed trace amount of Ga (0.70

152   at. %) may be attributed to Ga adsorption on boehmite. On the contrary, the spectrum (Fig. 1f)

153   collected from the darker nanoplate demonstrates that the O/Ga atomic ratio is also close to 2,

154   with 31 at. % of Ga and 68 at. % of O. A trace amount of Al (0.47 at. %) are evenly distributed

155   in the whole area, indicating that no obvious Al enrichment in Ga-rich phase. In addition, as

156   shown in Supplementary Fig. S2, the low magnification EDS analyses of the product

157   demonstrate that the Al/Ga atomic ratio is close to 10, indicating that the product is mainly

158   composed of boehmite, and the Ga-rich phase accounts for only a small part of it.

159   Figure 2 shows XRD pattern of the product. Besides those diffraction peaks (marked by

160   black dots) that can be indexed to boehmite, a series of new peaks (marked by red asterisks) at

161   2θ = 27.3, 37.2, 44.1, 47.2, 47.8, 53.6, 61.5, 62.1, 65.4 and 69.3° appear. Combined with the

162   mapping and EDS results (Fig. 1c-f), it follows that the new diffraction peaks should originate

163   from the Ga-rich phase in the product. It is worth noting that these diffraction peaks cannot be

164   indexed to any possible phase of known Al and/or Ga compounds. Interestingly, the new

165   peaks are always shifted towards higher d-spacings of each diffraction peak of boehmite

166   except for the (020) diffraction peak located at 2θ = 14.4°. As shown in the inset of Fig. 2, the

167   magnified XRD pattern in the 2θ range of 13-16° clearly reveal that the strongest diffraction

168   peak slightly shifts towards higher d-spacing compared to the (020) diffraction peak of

169   template boehmite. Considering that the lattice parameters of boehmite do not change after

170   reaction, the shifts can be attributed to the superposition of the (020) diffraction peak of

171   boehmite and a new diffraction peak. Generally, when foreign ions with a larger size are

172   incorporated into the lattice of host crystal, some interplanar spacings of the doped crystal

173   would increase. Correspondingly, the diffraction peaks shift to lower 2θ angles. Therefore, the

174   set of new diffraction peaks in Fig. 2 may derive from the Ga-substituted boehmite.

175   Combined with the STEM-EDS results, where the O/Ga atomic ratio of the new phase is close

176   to 2, consistent with O/Al atomic ratio of template boehmite, it can be concluded that the

177   Ga-rich phase in the product is isostructural with boehmite, with an ideal formula GaOOH.

178   In order to verify crystal structure of the Ga-rich phase, Rietveld analysis of the XRD

179   data was carried out using GSAS. Because the Ga-rich phase in the product is isostructural

180   with boehmite, the starting atomic parameters of the two phases (γ-AlOOH and Ga-rich phase)

181   in the product were both taken from those of boehmite. Figure 3 shows the refinement results,

182   and the corresponding refined lattice constants are presented in Table 1. The refinement

183   results indicate a good fit between the observed and calculated XRD patterns, with the final

184   refinement converging to the residual factor R_{wp} = 7.27% (Fig. 3). The good agreement with

185   boehmite indicate that the synthesized Ga oxyhydroxide is indeed isostructural with boehmite

186   (γ-AlOOH). The results listed in Table 1 also indicate that γ-AlOOH is 96.2% (mass fraction),

187   and Ga-rich phase is 3.8% in the product, which is consistent with EDS analyses (Fig. S2).

188   Moreover, the Ga-rich phase possesses lattice parameters of a = 3.8555 Å, b = 12.3287 Å, c =

189   2.9894 Å and V = 142.0995 $Å^3$ (Table 1), slightly larger than boehmite. These results further

190   support the XRD analyses (e.g., Fig. 2). Therefore, the Ga-rich phase can be referred to

191   γ-GaOOH.

192   The nanoscale structure of the intergrowth between boehmite template and growing Ga

193   oxyhydroxide was also determined through local atomic imaging of HAADF-STEM. For the

194   Al-rich phase, the high-resolution lattice fringes (Fig. 4a) have the *d* spacings 0.142, 0.202

195   and 0.231 nm in adjacent angles of 90° and 54°, and these values match with the d_{002}, d_{060} and

196   d_{031} of boehmite (JCPDS No. 21-1307) and their interfacial angles. In the case of Ga-rich

197   phase, as shown in Fig. 4b, two lattice fringes with spacings of 0.142 and 0.149 nm in an

198   angle of 61.3° were detected. These fringes are consistent with the calculated d_{171} and d_{002}

199   values of γ-GaOOH from the refinement. The SAED pattern (Fig. 4c) of the Al-rich phase

200   taken from area 1 in Fig 1a was also fully indexed to (002), (062), and (060) planes of

201   boehmite with [100] zone axis. Furthermore, the SAED pattern (e.g., Fig. 4d) of Ga-rich

202   phase taken from area 2 in Fig 1a shows the similar setting of diffraction spots to boehmite

203   (Fig. 4c), indicating that they have same crystal structures. The measured interplanar distances

8

204   of the Ga-rich phase are 0.150, 0.209 and 0.242 nm, corresponding to d_{002}, d_{060} and d_{031} of

205   γ-GaOOH oriented along the [100] zone axis according to the refinement results. These

206   values are about 3.5-5.5% larger than the lattice distances of d_{002}, d_{060} and d_{031} of boehmite

207   (0.142, 0.202 and 0.231 nm), consistent with the XRD results.

Formation mechanism of γ-GaOOH

209   The growth process of γ-GaOOH was tracked by characterizing the product using TEM

210   after keeping boehmite template in Ga^{3+} solution for different times. As shown in Fig.5, the

211   size of original nanosheets with lower brightness gradually decreases, indicating that the

212   boundary of boehmite template continuously dissolved with prolonging reaction time. After 1

213   day of reaction (Fig. 5b), many irregular small nanosheets with sizes from 10 to 40 nm and

214   lower brightness were formed and orientationally attached onto boehmite boundaries. As

215   reaction time extended to 3 days, the newly formed nanosheets grew into larger and perfect

216   nanosheets (100 nm to 300 nm) (e.g., Figs. 5c and 1a), indicating the unceasing growth of

217   γ-GaOOH. To identify the interfacial relationship between the boehmite template and the

218   growing Ga oxyhydroxide, the STEM-EDS mapping and line scanning at the intergrowth of

219   the two phases were conducted. According to the EDS line analysis results (Fig. 6a), there is a

220   clear transition of elements Ga and Al between γ-GaOOH and boehmite template, which

221   corresponds to an interface between the two phases. Moreover, Fig. 6c-f clearly shows the

222   spatial distribution of Ga and Al, where Ga was confined to the upper left corner of the

223   sample, and Al was detected only in the lower right corner of the sample, indicating that the

224   γ-GaOOH grew on specific crystallographic planes of boehmite template and no obvious

225   atomic substitution occurred in both phases. Based on the above experimental results and the

226   former crystal structure analysis for γ-GaOOH and boehmite, an epitaxial growth mechanism

227   for γ-GaOOH is proposed. As depicted in Fig. 7. First, boehmite would be partially dissolved

228   under initial acid conditions. Second, because of the same unit cell properties of γ-GaOOH

229   and γ-AlOOH, Ga can preferentially deposit on boehmite grain boundary as γ-GaOOH instead

230   of Al during boehmite dissolution process, where the local concentrations of OH^- and the

231   supersaturation degree for γ-GaOOH in the diffusion layer of boehmite template are higher

232   than those in the bulk solution. Therefore, the nucleation of γ-GaOOH on the edges of

9

233   boehmite is easier than that in the bulk solution. Third, as the reaction continues, the

234   γ-GaOOH can further nucleate and grow on the boehmite template via secondary nucleation

235   and epitaxial growth. In addition, the synthesis experiments with the temperature ranging

236   from 60 to 150 ℃ also demonstrate that γ-GaOOH can be obtained over a wide temperature

237   range, as shown in Supplementary Fig S3. In contrast, no γ-GaOOH was produced without

238   boehmite template in the control experiments. In particular, when using diaspore

239   (orthorhombic, space group *Cmcm*), gibbsite (monoclinic, space group *P2₁/c*) and corundum

240   (rhombohedral, space group $R\bar{3}c$) as the template, no γ-GaOOH can be obtained, indicating

241   that the lattice match is pivotal to the formation of Ga oxyhydroxide, which further supports

242   the boehmite template-based heteroepitaxial growth to control the formation of γ-GaOOH.

Implications

244   Ga is a moderately incompatible element, and behaves like Al during magmatic

245   differentiation and supergene geochemical process (e.g., de Argollo and Schilling, 1978;

246   McDonough, 1990; Wen et al., 2021). Although natural Ga reserves are relatively substantial,

247   Ga rarely forms independent or high-content minerals. It usually disperses in small amounts

248   in some minerals and substitutes for elements such as Al and Zn (U.S. Geological Survey,

249   2021). The distribution of Ga among different mineral phases depends on numerous factors

250   including strong bonding of Ga with organic matter (e.g., graphite), isomorphism with Al, Fe

251   and Zn, and adsorption on clay minerals and iron oxides (Yuan et al., 2021). Most Ga

252   incorporated into clay minerals is inherited from feldspars and micaceous minerals

253   undergoing weathering, where Ga and Al behave identically through the series of mineral

254   transformations from feldspar to kaolin or gibbsite (Gilkes et al., 1973). Moreover, Ga-Al

255   fractionation can also occur under extreme weathering conditions (Young and Nesbitt, 1998).

256   For example, the average Ga/Al ratio in saprolite (2.1×10^{-4}) is lower than that of the regolith

257   for basaltic weathering (2.6×10^{-4}) (Hieronymus et al., 2001). Nevertheless, Ga is usually

258   enriched in Al ore deposit such as bauxite, which contributes 90% of current industrial Ga.

259   Boehmite, as the main Al species in bauxite, as well as the precursor of diaspore, is the most

260   important carrier of Ga (Schulte et al., 2014; Abedini et al., 2019). In addition, boehmite in

10

261 coal was also reported to be enriched in Ga, with some of them far higher than the Ga

262 industrial grade (30 $\mu g \cdot g^{-1}$) (Dai et al., 2006a, 2008, 2012; Wang et al., 2011; Sun et al., 2013).

263 However, limited information is available concerning the studies of Ga in boehmite. Our

264 results provide insight into the incorporation of Ga in boehmite, and indicate that boehmite

265 can act as a structure template to enrich free Ga, and epitaxially induce nucleation and growth

266 of γ-GaOOH. This process occurred at as low as 60°C, which matches with the formation

267 conditions of bauxites and coal-related boehmite to a certain extent. Therefore, it can be

268 anticipated that γ-GaOOH as a potential Ga mineral is concomitant with boehmite in nature.

269 Our study also provides a potential migration, enrichment and mineralization mechanism of

270 Ga, which will improve the understanding of the geochemical processes and occurrence of Ga

271 in nature.

272 ## Acknowledgements

References

277

278   Abedini, A., Khosravi, M., and Calagari, A.A. (2019) Geochemical characteristics of the

279   Arbanos karst-type bauxite deposit, NW Iran: implications for parental affinity and factors

280   controlling the distribution of elements. Journal of Geochemical Exploration, 200, 249–

281   265.

282   Bielowicz, B. (2020) Ash Characteristics and Selected Critical Elements (Ga, Sc, V) in Coal

283   and Ash in Polish Deposits. Resources, 9(9), 115.

284   Braniste, T., Dragoman, M., Zhukov, S., Aldrigo, M., Ciobanu, V., Iordanescu, S., Liudmila,

285   A., Francesco, F., Giacomo, C., Simion, R., Fabian, S., Rainer, A., Pascal, C., Boris, G., and

286   Tiginyanu, I. (2020) Aero-Ga_2O_3 Nanomaterial Electromagnetically Transparent from

287   Microwaves to Terahertz for Internet of Things Applications. Nanomaterials, 10(6), 1047.

288   Christoph G.G., Corbató C.E., Hofmann D.A., and Tettenhorst R.T. (1979) The crystal

289   structure of boehmite. Clays and clay minerals, 27(2), 81–86.

290   Corathers L.A., and Manganese U. (2017) Mineral commodity summaries. U.S. Geological

291   Survey, 106–107.

292   Dai, S.F., Jiang, Y.F., Ward, C.R., Gu, L.D., Seredin, V.V., Liu, H.D., Zhou, D., Wang, X.B.,

293   Sun, Y.Z. Zou, J.H., and Ren, D.Y. (2012) Mineralogical and geochemical compositions of

294   the coal in the Guanbanwusu Mine, Inner Mongolia, China: further evidence for the

295   existence of an Al (Ga and REE) ore deposit in the Jungar Coalfield. International Journal

296   of Coal Geology, 98, 10–40.

297   Dai, S.F., Li, D., Chou, C.L., Zhao, L., Zhang, Y., Ren, D.Y., Ma, Y.W., and Sun, Y.Y. (2008)

298   Mineralogy and geochemistry of boehmite-rich coals: new insights from the Haerwusu

299   Surface Mine, Jungar Coalfield, Inner Mongolia, China. International Journal of Coal

300   Geology, 74, 185–202.

301   Dai, S.F., Ren, D.Y., and Li, S.S. (2006b) Discovery of the superlarge gallium ore deposit in

302   Jungar, Inner Mongolia, North China. China Science Bulletin, 51, 2243–2252.

303   Dai, S.F., Ren, D.Y., Chou, C.L., Li, S.S., and Jiang, Y.F. (2006a) Mineralogy and

304   geochemistry of the No. 6 Coal (Pennsylvanian) in the Junger Coalfield, Ordos Basin,

305   China. International Journal of Coal Geology, 66, 253–270.

306   de Argollo, R.M., and Schilling, J.G. (1978) Ge/Si and Ga/Al variations along the Reykjanes

307   ridge and Iceland. Nature, 276(5683), 24–28.

308   Dubey, S.P., Dwivedi, A.D., Sillanpää, M., Lee, H., Kwon, Y.N., and Lee, C. (2017)

309   Adsorption of As(V) by boehmite and alumina of different morphologies prepared under

310   hydrothermal conditions. Chemosphere, 169, 99–106.

311   Eheliyagoda, D., Zeng, X., Wang, Z., Albalghiti, E., and Li, J. (2019) Forecasting the

312   temporal stock generation and recycling potential of metals towards a sustainable future:

313   The case of gallium in China. Science of Total Environment, 689, 332–340.

314   Foley, N.K., Jaskula, B.W., Kimball, B.E., and Schulte, R.F. (2017) Gallium. In K.J. Schulz,

315   J.H. DeYoung Jr., R.R. Seal II, and D.C. Bradley, Ed., Critical mineral resources of the

316   United States—economic and environmental geology and prospects for future supply, p.

317   H1–H35. U.S. Geological Survey, Virginia.

318   Frenzel, M., Ketris, M.P., Seifert, T., and Gutzmer, J. (2016) On the current and future

319   availability of gallium. Resources Policy, 47, 38–50.

320   Gilkes, R.J., Scholz, G., and Dimmock, G.M. (1973) Lateritic deep weathering of granite.

321   Journal of Soil Science, 24(4), 523–536.

322   Gladyshev, S.V., Akcil, A., Abdulvaliyev, R.A., Tastanov, E.A., Beisembekova, K.O.,

323   Temirova, S.S., and Deveci, H.A.C.I. (2015) Recovery of vanadium and gallium from solid

324   waste by-products of Bayer process. Mineral Engineering, 74, 91–98.

325   Hieronymus, B., Kotschoubey, B., and Boulègue, J. (2001) Gallium behaviour in some

326   contrasting lateritic profiles from Cameroon and Brazil. Journal of Geochemical

327   Exploration, 72, 147–163.

328   Ji, W.T., Xie, K.Q., Huang, H.Y., and Chen, H.L. (2021) Recovery of gallium from yellow

329   phosphorus flue dust by vacuum carbothermal reduction. Journal of Cleaner Production,

330   284, 124706.

331   Ji, W.T., Xie, K.Q., Yan, S.Y., Huang, H.Y., and Chen, H.L. (2020) A new method of recycling

332   gallium from yellow phosphorus flue dust by vacuum thermal reduction process. Journal of

333   Hazardous Materials, 400, 123234.

334   Kato, C., Moynier, F., Foriel, J., Teng, F.Z., and Puchtel, I.S. (2017) The gallium isotopic

335   composition of the bulk silicate Earth. Chemical Geology, 448, 164–172.

336   Lu, F.H., Xiao, T.F., Lin, J., Ning, Z.P., Long, Q., Xiao, L.H., Huang F., Wang, W.K., Xiao,

337   Q.X., Lan, X.L., and Chen, H.Y. (2017) Resources and extraction of gallium: A review.

338   Hydrometallurgy, 174, 105–115.

339   Lv, G.S., Chen, W.H., Liu, X., and Feng, Z.H. (2019) A dual-band GaN MMIC power

340   amplifier with hybrid operating modes for 5G application. IEEE Microwave and Wireless

341   Components Letters, 29(3), 228–230.

342   Maarefvand M., Sheibani S., and Rashchi F. (2020) Recovery of gallium from waste LEDs by

343   oxidation and subsequent leaching. Hydrometallurgy, 191, 105230.

344   Mastalerz, M., and Drobniak, A. (2012) Gallium and germanium in selected Indiana coals.

345   International Journal of Coal Geology, 94, 302–313.

346   McDonough, W.F. (1990) Comment on "Abundance and distribution of gallium in some

347   spinel and garnet lherzolites" by DB McKay and RH Mitchell. Geochimica et

348   Cosmochimica Acta, 54(2), 471–473.

349   Qiao, J.W., Li, C.C., Fan, Q., Tan, J., Xie, T., Yang, C., and Lv, J. (2016) Characteristics of

350   coal resources and their geological background at northern Qinghai Tibet Plateau. Journal

351   of the China Coal Society, 41(2), 294–302 (In Chinese).

352   Qin, S.J., Sun, Y.Z., Li, Y.H., Wang, J.X., Zhao, C.L., and Gao, K. (2015) Coal deposits as

353   promising alternative sources for gallium. Earth Science Reviews, 150, 95–101.

354   Ramanujam J., and Singh U.P. (2017) Copper indium gallium selenide based solar cells–a

355   review. Energy & Environmental Science, 10(6), 1306–1319.

356   Rytuba J.J, Bliss J.D, Moyle P.R, and Long, K.R. (2003) Hydrothermal Enrichment of

357   Gallium in Zones of Advanced Argillic Alteration, Examples from the Paradise Peak and

358   McDermitt Ore Deposits, Nevada. U.S. Geological Survey.

359   Saikia, B.K., Ward, C.R., Oliveira, M.L., Hower, J.C., De Leao, F., Johnston, M.N., O'Bryan,

360   A., Sharma, A., Baruah, B.P., and Silva, L.F. (2015) Geochemistry and nano-mineralogy of

361   feed coals, mine overburden, and coal–derived fly ashes from Assam (North-east India): a

362   multi-faceted analytical approach. International Journal of Coal Geology, 137, 19–37.

363   Schulte R.F., and Foley N.K. (2014) Compilation of gallium resource data for bauxite

364   deposits. U.S. Geological Survey.

365   Schulz, K.J., DeYoung Jr., J.H., Seal II, R.R., and Bradley, D.C. (2017) Critical mineral

366   resources of the United States—Economic and environmental geology and prospects for

367   future supply. U.S. Geological Survey.

368   Seredin, V.V., Dai, S., Sun, Y., and Chekryzhov, I.Y. (2013) Coal deposits as promising

369   sources of rare metals for alternative power and energy-efficient technologies. Applied

370   Geochemistry, 31, 1–11.

371   Shao, P., Wang, W.F., Chen, L., Duan, P.P., Qian, F.C., Ma, M.Y., Xiong, W. H., and Yu, S.

372   (2018) Distribution, occurrence, and enrichment of gallium in the Middle Jurassic coals of

373   the Muli Coalfield, Qinghai, China. Journal of Geochemical Exploration, 185, 116–129.

374   Sun, Y.Z., Zhao, C.L., Zhang, J.Y., Yang, J.J., Zhang, Y.Z., Yuan, Y., Xu, J., and Duan, D.J.

375   (2013) Concentrations of valuable elements of the coals from the Pingshuo Mining District,

376   Ningwu Coalfield, northern China. Energy Exploration & Exploitation, 31(5), 727–744.

377   Sutter, E., French, J.S., Sutter, S., Idrobo, J.C., and Sutter, P. (2020) Vapor–liquid–solid

378   growth and optoelectronics of gallium sulfide van der Waals nanowires. ACS nano, 14(5),

379   6117–6126.

380   U.S. Geological Survey. (2021) Mineral Commodity Summaries: USGS Unnumbered Series.

381   Wang, W., Qin, Y., Liu, X., Zhao, J., Wang, J., Wu, G., and Liu, J. (2011) Distribution,

382   occurrence and enrichment causes of gallium in coals from the Jungar Coalfield, Inner

383   Mongolia. Science China-Earth Sciences, 54, 1053–1068.

384   Wen J., Zhang Y.X., Wen H.J., Ling, K.Y., Zhu, C.W., Fan, H.F., and Shen, N.P. (2021)

385   Gallium isotope fractionation in the iaoshanba bauxite deposit, central Guizhou Province,

386   southwestern China. Ore Geology Reviews, 137, 104299.

387   Xue, B., Wei, B.T., Ruan, L.X., Li, F.F., Jiang, Y.S., Tian, W.J., Su, B., and Zhou, L.M. (2019)

388   The influencing factor study on the extraction of gallium from red mud. Hydrometallurgy,

389   186, 91–97.

390   Young, G.M., and Nesbitt, H.W. (1998) Processes controlling the distribution of Ti and Al in

391   weathering profiles, siliciclastic sediments and sedimentary rocks. Journal of Sedimentary

392   research, 68(3), 448–455.

393   Yuan, W., Chen, J.B., Teng, H., Chetelat, B., Cai, H.M., Liu, J.C., Wang, Z.C., Bouchez, J.L.,

394   Moynier, F., Gaillardet, J., Schott, J., and Liu, C. (2021) A review on the elemental and

395   isotopic geochemistry of Gallium. Global Biogeochemical Cycles, 35(9), e2021GB007033.

396   Zhan, L., Zhang, Y.L., Ahmad, Z., and Xu, Z.M. (2020) Novel recycle technology for

397   recovering gallium arsenide from scraped integrated circuits. ACS Sustainable Chemistry

398   & Engineering, 8(7), 2874–2882.

399   Zhao, C.L., Qin, S.J., Yang, Y.C., Li, Y.H., and Lin, M.Y. (2009) Concentration of gallium in

400   the Permo-Carboniferous coals of China. Energy Exploration & Exploitation, 27, 333–343.

401   Zhao, Z.S., Cui, L., Guo, Y.X., Li, H.Q., and Cheng, F.Q. (2020) Recovery of gallium from

402   sulfuric acid leach liquor of coal fly ash by stepwise separation using P507 and Cyanex 272.

403   Chemical Engineering Journal, 381, 122699.

404   Zhou, J.B., Zhuang, X.G., Alastuey, A., Querol, X., and Li, J.H. (2010) Geochemistry and

405   mineralogy of coal in the recently explored Zhundong large coal field in the Junggar basin,

406   Xinjiang province, China. International Journal of Coal Geology, 82, 51–67.

407

408

409

410   **Table 1** Structural parameters and phase fractions of γ-GaOOH and boehmite in the product

411   obtained from Rietveld analysis of XRD data

Sample	Lattice Parameters (Sigmas)	Atomic positions				Uiso (Sigmas)	Fraction of phase (Sigmas)
		Atom	x	y (Sigmas)	z		
Boehmite	a = 3.7116 Å (0.000224)	Al	0.25	0.683 (0.000215)	0	0.08859 Å^2 (0.090000)	96.2% (0.000063)
	b = 12.2284 Å (0.000793)	O1	0.25	0.287 (0.000252)	0	0.04505 Å^2 (0.091000)	
	c = 2.8699 Å (0.000216)	O2	0.25	0.080 (0.000295)	0	0.05739 Å^2 (0.106000)	
	V = 130.259 Å^3						
γ-GaOOH	a = 3.8555 Å (0.000478)	Ga	0.25	0.672 (0.000374)	0	0.02636 Å^2 (0.112000)	3.8% (0.000280)
	b = 12.3287 Å (0.002090)	O1	0.25	0.288 (0.001127)	0	0.02347 Å^2 (0.565000)	
	c = 2.9894 Å (0.000480)	O2	0.25	0.080 (0.001134)	0	0.02849 Å^2 (0.569000)	
	V = 142.099 Å^3						

412

Figure Captions

413

414 Fig. 1 TEM images of the synthesized product (a) and template boehmite (b), STEM-EDS

415   elemental mappings (c-d) and EDS spectra (e-f) of the synthesized product.

416 Fig. 2 Representative XRD pattern for the synthesized product. Inset in Fig. 2: local

417   zoomed-in of the XRD pattern over 2θ range of 13-16°.

418 Fig. 3 Rietveld analysis of XRD data for the synthesized product.

419 Fig. 4 Atomic-resolution HAADF-STEM images (a and b) and selected area electron

420   diffraction (SAED) patterns (c and d) collected from areas 1 and 2 in Fig. 1a.

421 Fig. 5 TEM images of boehmite (a) and boehmite after 1(b) and 3 days (c) of reaction.

422 Fig. 6 HAADF-STEM image and STEM-EDS line scanning (a) and corresponding

423   STEM-EDS elemental mappings (c-d) at the intergrowth of the two phases in the

424   product.

425 Fig. 7 Schematic representation of the proposed formation mechanism for γ-GaOOH.

426

427

428

Fig. 1

429

430
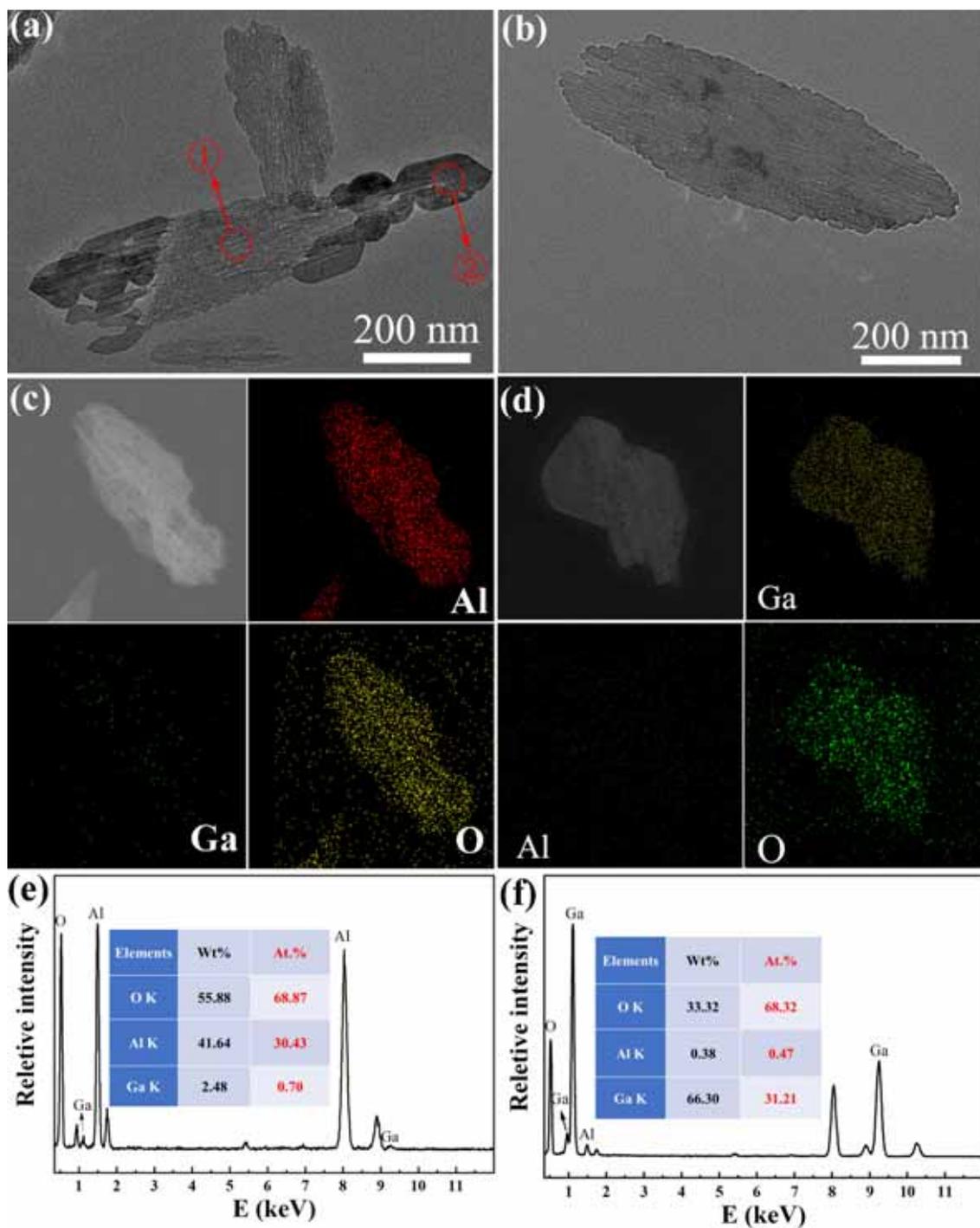
431

432

433

434

435

436

437

438

439

440

441

442
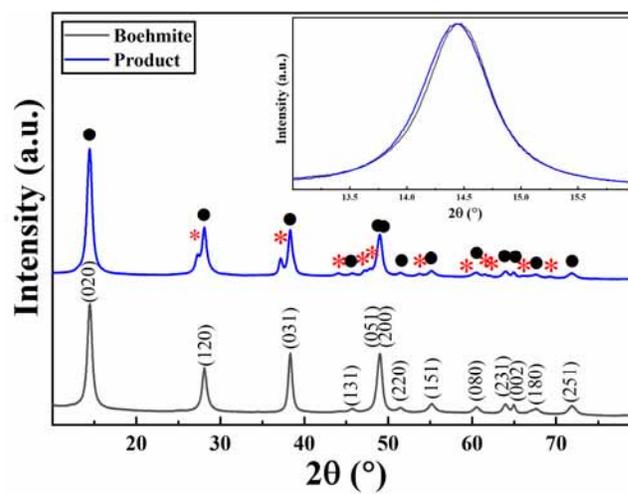
Fig. 2

444

445
446
447
448
449
450
451
452
453
454
455
456
457
458
459
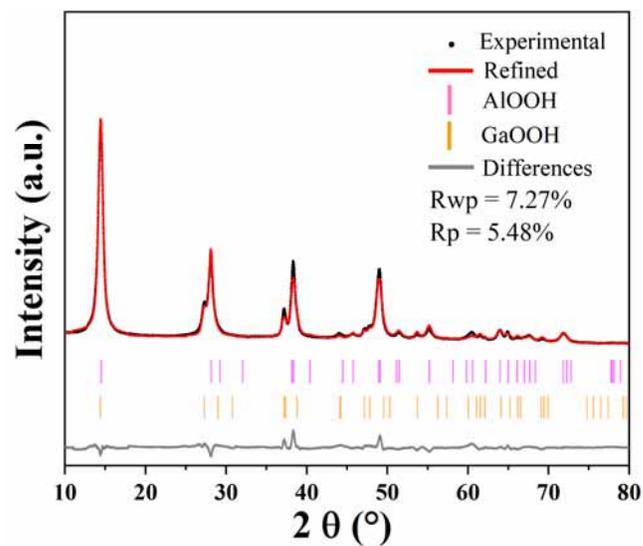
460

461   **Fig. 3**

462

463

464

465

466

467

Fig. 4

468

469
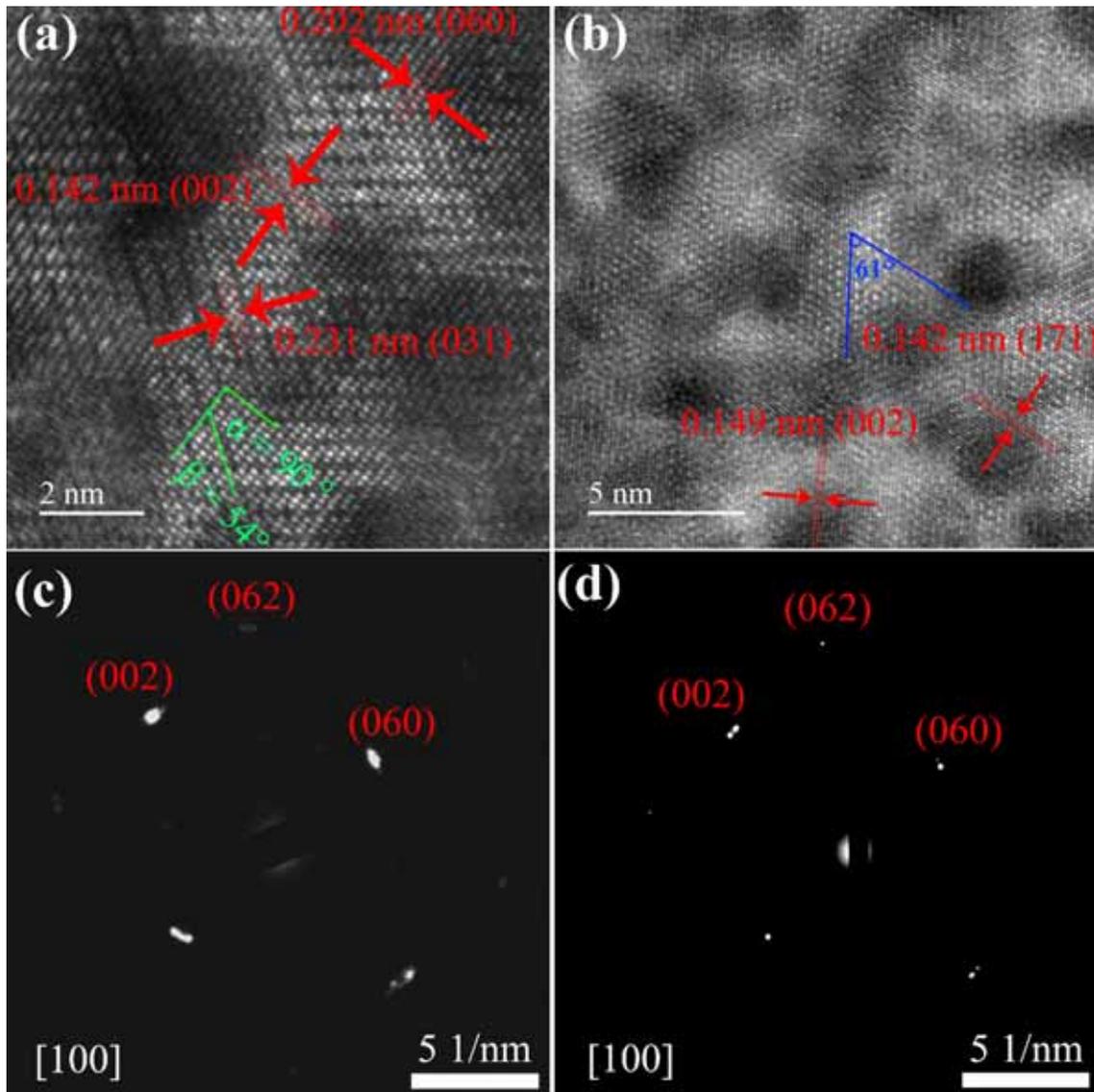
470
471
472
473
474
475
476
477
478
479
480
481
482
483
484
485
486
487
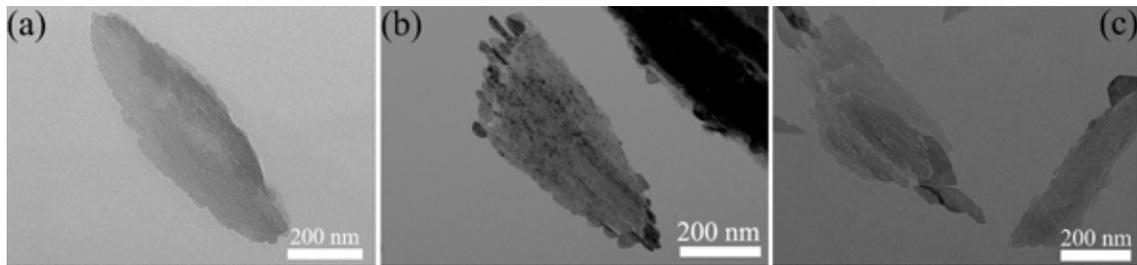
488

Fig. 5

489

490

491

492

493

494
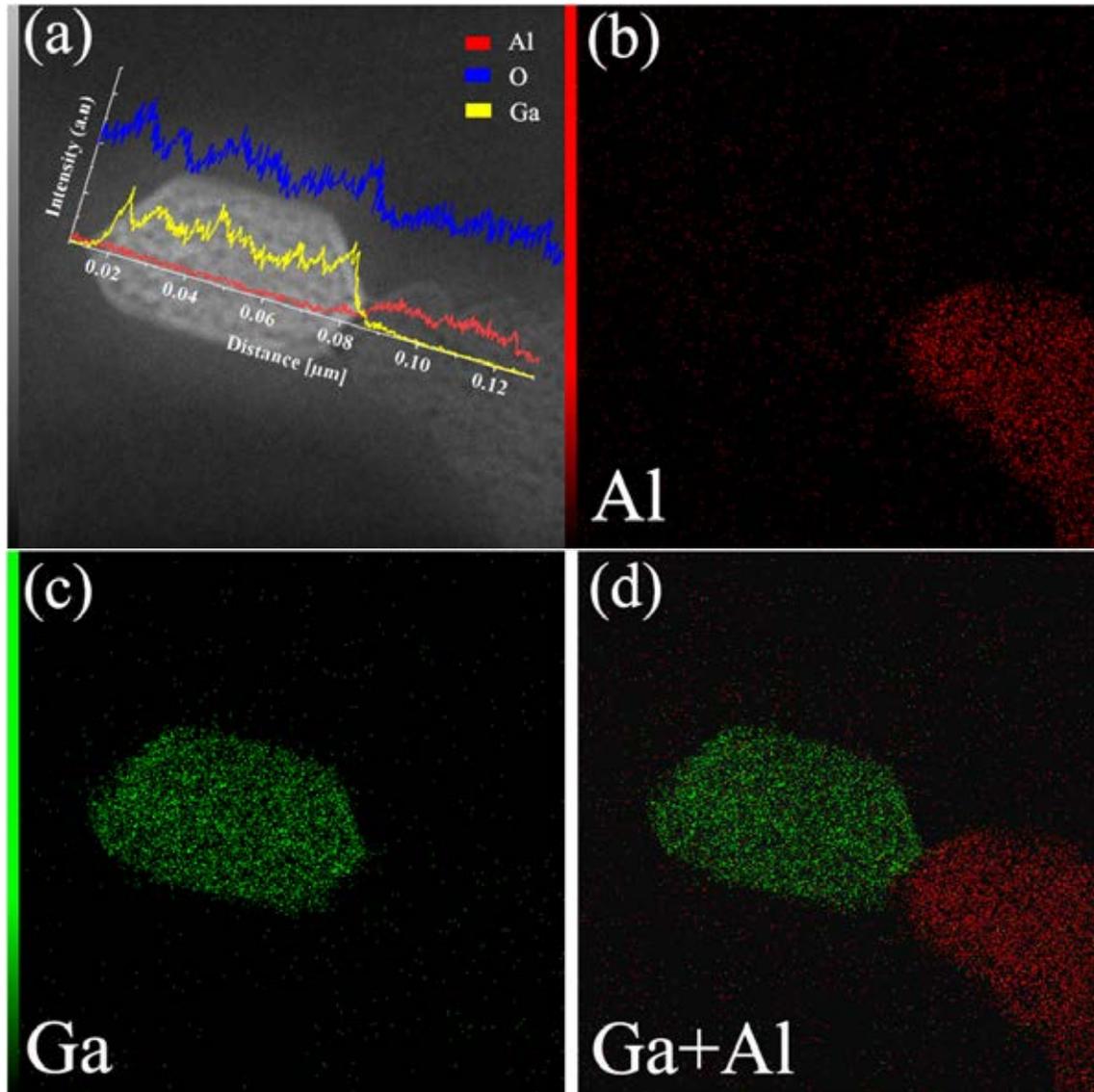
Fig. 6

496

497

498

499

500

501

502

503

504

505

506

507

Fig. 7

508

509